ADVANCED MATERIALS

Supporting Information

for *Adv. Mater.*, DOI: 10.1002/adma.201401757

Water-Free Titania-Bronze Thin Films with Superfast Lithium-Ion Transport

*Kui Zhang, Michael B. Katz, Baihai Li, Sung Joo Kim, Xianfeng Du, Xiaoguang Hao, Jacob R. Jokisaari, Shuyi Zhang, George W. Graham, Anton Van der Ven, Bart M. Bartlett, and Xiaoqing Pan**

Supporting Information for *Adv. Mater.*, DOI: 10.1002/adma.201401757.

Water-free Titania-Bronze Thin Films with Superfast Lithium Ion Transport

Kui Zhang, Michael B. Katz, Baihai Li, Sung Joo Kim, Xianfeng Du, Xiaoguang Hao, Jacob R. Jokisaari, Shuyi Zhang, George W. Graham, Anton Van der Ven[†], Bart M. Bartlett, and Xiaoqing Pan[*]

K. Zhang, Dr. M. B. Katz, Dr. B. H. Li, S. J. Kim, Dr. X. F. Du, J. R. Jokisaari, S. Y. Zhang, Prof. G. W. Graham, Prof. A. Van der Ven, Prof. X. Q. Pan
Department of Materials Science and Engineering
University of Michigan, Ann Arbor, MI 48109, USA
E-mail: panx@umich.edu

X. G. Hao, Prof. B. M. Bartlett
Department of Chemistry
University of Michigan, Ann Arbor, MI 48109, USA

[†] Presently at Materials Department, University of California – Santa Barbara, CA 93106, USA

I. Crystal structures of TiO_2-B and Ca:TiO_2-B

Figure 1 shows the crystal structures of both regular TiO_2-B and its variant Ca:TiO_2-B phases. Although the extra Ca atoms make the latter more complicated, there is still a strong resemblance between the two. The STEM images in Figure 2b and 2d can be clearly associated with the two atomic structures projected along the [010] direction in the center column of Figure 1. The geometric model of the novel Ca:TiO_2-B phase has been refined by analyzing the HR-STEM images and performing first-principles optimization. Table S1 lists in detail the atom positions in the Ca:TiO_2-B structure.

By visual inspection, the channels running along the *b*-axis appear to be most open among the three crystallographic axes in both two structures, and may be a good candidate for high Li^+ mobility in the crystal. Channels parallel to various other directions can also be found by manipulating the model. It is worth noting that more rigorous study than simply observing the cross sectional areas of the channel opening is required to determine with relative certainty the actual diffusion path that is most energetically favorable for fast Li^+ transport,[1] as the results may be counter-intuitive. The ability to fabricate crystalline thin films of the active storage material with well-defined lattice plane on the surface, such as what we have demonstrated in this report, is therefore of great value to experimentally determine the preferred Li^+ pathways.

Table S1. Atom positions in the Ca:TiO_2-B structure.

#	*Atom*		*x*	*y*	*z*	*#*	*Atom*		*x*	*y*	*z*
1	O	O1	0.19999	0.93727	0.34267	35	O	O35	0.44389	0.43501	0.48876
2	O	O2	0.04096	0.93438	0.98907	36	O	O36	0.19931	0.93896	0.49221
3	O	O3	0.23305	0.93649	0.11333	37	O	O37	0.54041	0.4367	0.84527
4	O	O4	0.07177	0.93646	0.21254	38	O	O38	0.28431	0.43673	0.8422
5	O	O5	0.38543	0.93642	0.24343	39	O	O39	0.03923	0.93309	0.84518
6	O	O6	0.7005	0.43782	0.34213	40	O	O40	0.78454	0.93558	0.84229
7	O	O7	0.53992	0.43719	0.98906	41	O	O41	0.5666	0.93536	0.41677
8	O	O8	0.73327	0.43714	0.11332	42	O	O42	0.41789	0.93805	0.91639
9	O	O9	0.57158	0.43772	0.2121	43	O	O43	0.91796	0.43314	0.91749
10	O	O10	0.88567	0.43771	0.24335	44	O	O44	0.06658	0.43879	0.41808
11	O	O11	0.78487	0.9355	0.99189	45	Ti	Ti1	0.22043	0.93658	0.24214
12	O	O12	0.94481	0.93819	0.34546	46	Ti	Ti2	0.06116	0.93641	0.09019
13	O	O13	0.75278	0.93744	0.22097	47	Ti	Ti3	0.72074	0.43715	0.24147
14	O	O14	0.91413	0.93789	0.12209	48	Ti	Ti4	0.56112	0.43659	0.09009
15	O	O15	0.6003	0.93703	0.09083	49	Ti	Ti5	0.76538	0.93697	0.09239
16	O	O16	0.28498	0.43691	0.9919	50	Ti	Ti6	0.92466	0.93757	0.2442
17	O	O17	0.44504	0.43607	0.34505	51	Ti	Ti7	0.26493	0.43673	0.09246
18	O	O18	0.25261	0.43655	0.22121	52	Ti	Ti8	0.42448	0.43642	0.24382
19	O	O19	0.41393	0.43555	0.1219	53	Ti	Ti9	0.21922	0.93567	0.59265
20	O	O20	0.09999	0.43618	0.0913	54	Ti	Ti10	0.06009	0.93443	0.74408
21	O	O21	0.23209	0.93441	0.72099	55	Ti	Ti11	0.71913	0.43538	0.59214
22	O	O22	0.07037	0.93436	0.62223	56	Ti	Ti12	0.56028	0.43575	0.74408
23	O	O23	0.38436	0.93492	0.59074	57	Ti	Ti13	0.26434	0.43449	0.7417
24	O	O24	0.73211	0.43547	0.72103	58	Ti	Ti14	0.42346	0.43479	0.58992
25	O	O25	0.57044	0.43497	0.62189	59	Ti	Ti15	0.76407	0.93521	0.74178
26	O	O26	0.88417	0.43548	0.59087	60	Ti	Ti16	0.9231	0.93527	0.59028
27	O	O27	0.75136	0.93542	0.61322	61	Ti	Ti17	0.58362	0.45134	0.41619
28	O	O28	0.2515	0.43522	0.61321	62	Ti	Ti18	0.40087	0.42763	0.91679
29	O	O29	0.41305	0.43458	0.71227	63	Ti	Ti19	0.90097	0.9446	0.91686
30	O	O30	0.0992	0.43408	0.74361	64	Ti	Ti20	0.08325	0.93465	0.41732
31	O	O31	0.91301	0.93537	0.71234	65	Ca	Ca1	0.87195	0.43614	0.41755
32	O	O32	0.59921	0.93577	0.74336	66	Ca	Ca2	0.37179	0.93857	0.41769
33	O	O33	0.94383	0.9365	0.48925	67	Ca	Ca3	0.61261	0.93498	0.91722
34	O	O34	0.69927	0.43558	0.49164	68	Ca	Ca4	0.11262	0.43539	0.91721

II. Microstructure of the as-grown thin films

Both the Ca:TiO_2-B film and the TiO_2-B/Ca:TiO_2-B dual layer film have fairly smooth surfaces on the *a*-*b* plane due to the characteristically layered structure of bronze, as shown in Figure S1. Crystal defects including grain boundaries, dislocations and stacking faults can be identified. More detailed investigation into various structural features and forming mechanism in the thin films is currently underway.

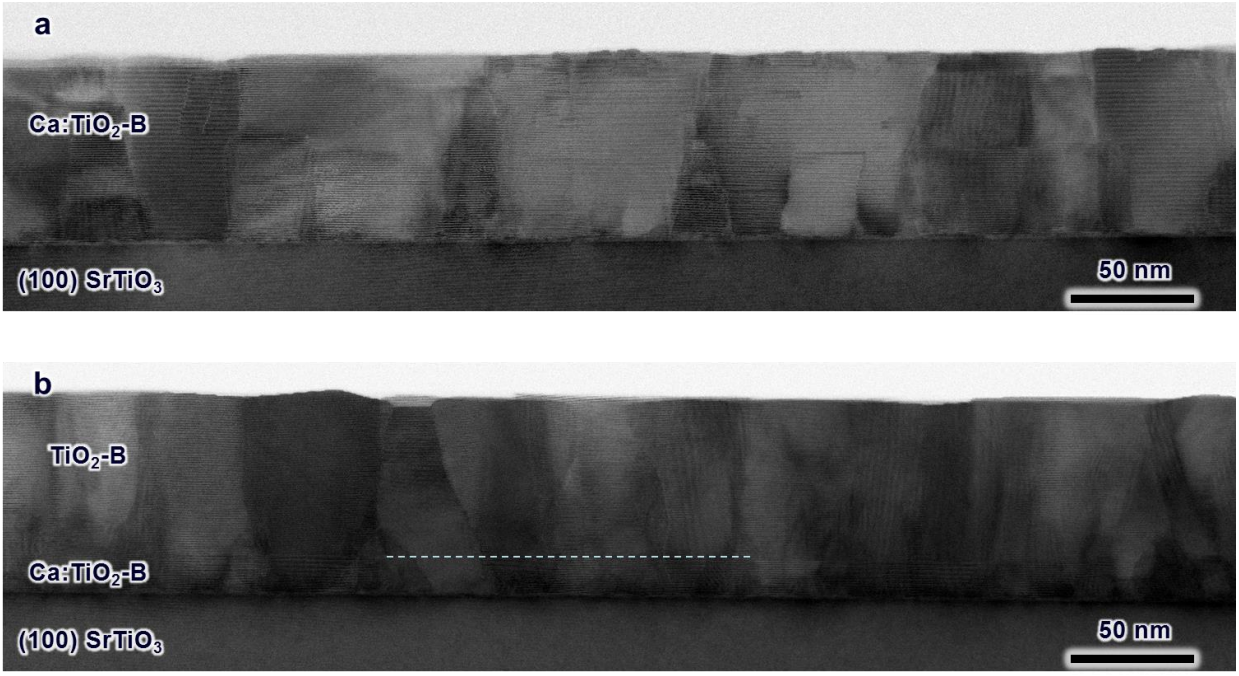

Figure S1. As-grown morphology of both the Ca:TiO_2 thin film and the TiO_2-B/Ca:TiO_2-B dual layer film on (100) $SrTiO_3$ substrate. a) Low magnification STEM image of a Ca:TiO_2-B film with ~75 nm thickness. b) Low magnification STEM image of a TiO_2-B film (~65 nm) grown on top of a thin Ca:TiO_2-B template layer (~15 nm). The dash line was drawn to locate the interface.

III. Experimental details for electrochemical measurements on the thin films

In order to investigate the electrochemical performance of the thin films, a current collector is needed, either on top or at the bottom of the film. Conductive $SrTiO_3$ substrates doped with 0.5 at.% Nb (resistivity 0.05 Ω cm) were used as bottom current collectors, and we found that they provided similar film quality to the ones grown on undoped $SrTiO_3$ substrates. Conversely, for films grown on non-conductive $SrTiO_3$ substrates, a top current collection geometry was fabricated using a grid of Cu wires with line width of 100 μm and a thickness of 20 nm which were deposited on the film surface in an E-beam evaporator with a Mo mask. On a 10×10 mm^2 test sample, the grid covers <0.8% of the surface area, which should have a negligible influence on the Li^+ exchange between the film and the electrolyte. Such a configuration is shown schematically in Figure S2.

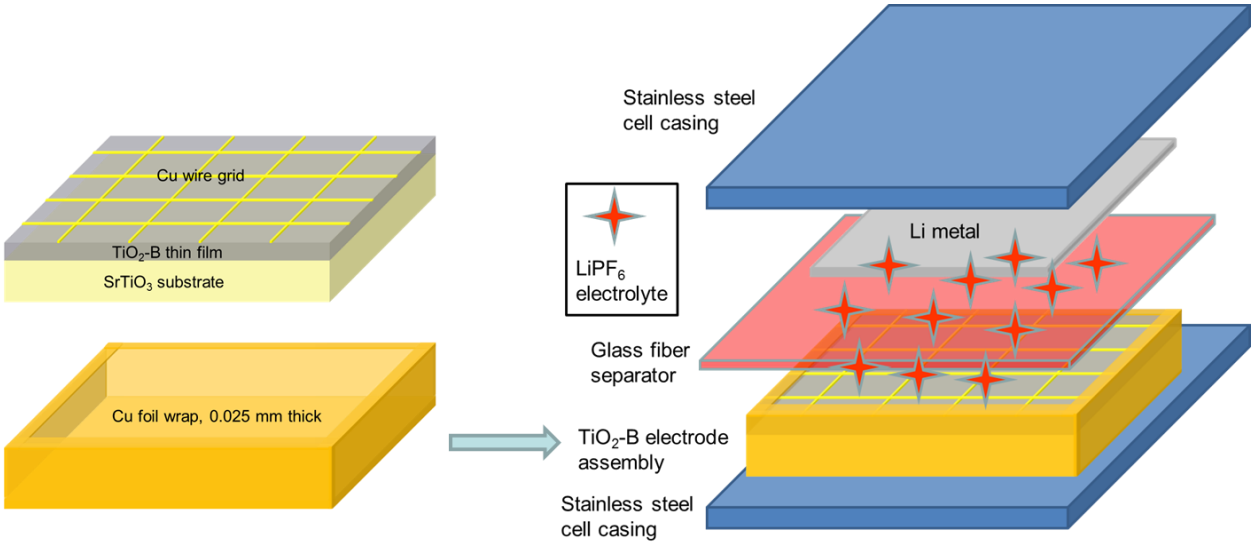

Figure S2. Top current collector configuration for electrochemical measurements. All battery performance results reported in the paper were acquired using such configuration from films grown on insulating 10×10 mm^2 $SrTiO_3$ substrates.

While using conductive Nb:$SrTiO_3$ substrate as bottom current collector, electrons are traveling through the entire substrate to the external circuit, and therefore the electrochemical force may drive some Li^+ into the substrate. Even though $SrTiO_3$ does not appear to have a high Li^+

capacity,[2] it is important to rule out the contribution from the substrate for determining the actual capacity of the film. A bare Nb:$SrTiO_3$ substrate was assembled in a half-cell and tested with exactly the same routine and rates as for the thin film samples. The measured capacity of the substrate at each rate was then subtracted from the total to obtain the capacity of the film at that rate. It should be noted that the voltage window of 1-3 V for TiO_2-B film testing is much higher than the possible Li intercalation voltage of $SrTiO_3$,[2] so the substrate contribution is very low, as seen in the control test at a 1C rate below (Figure S3).

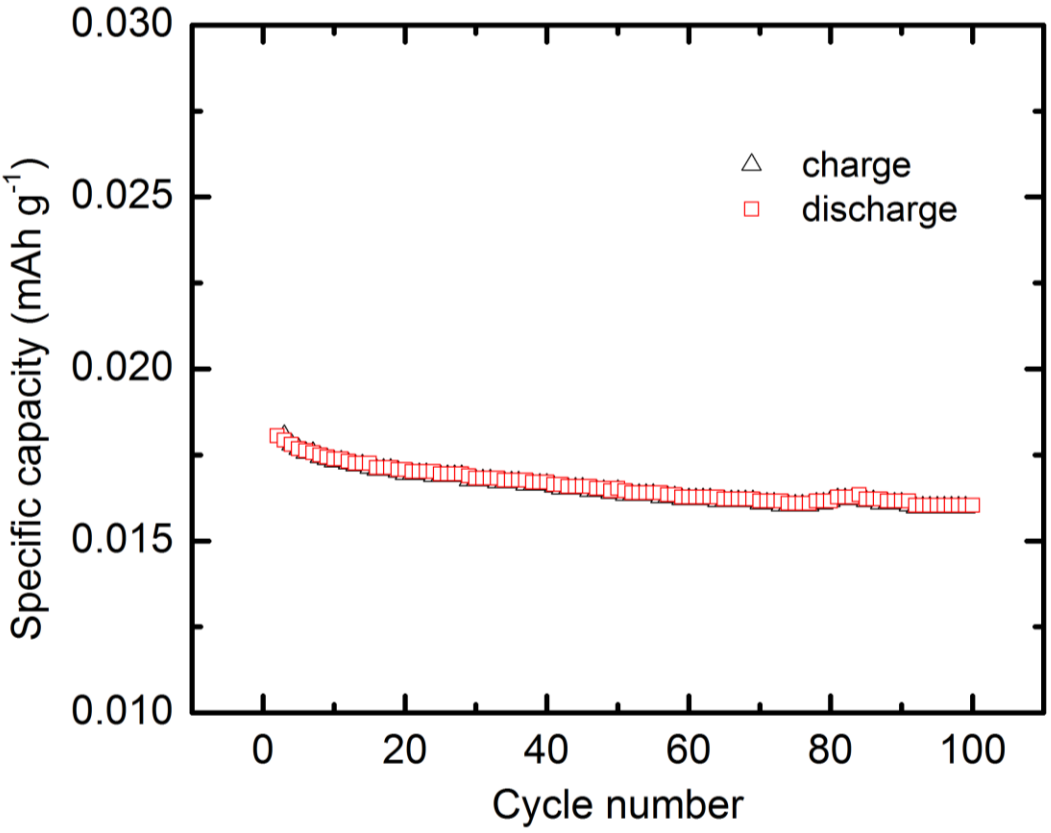

Figure S3. Cycling performance of a bare Nb:$SrTiO_3$ (100) substrate at a 1C rate for 100 cycles in a voltage window of 1-3 V versus Li metal.

A similar approach is needed to determine the capacity of the regular TiO_2-B phase. Since the TiO_2-B film has to be grown on top of a Ca:TiO_2-B template layer, our procedure for figuring its specific capacity was to cycle the Ca:TiO_2-B sample and the TiO_2-B/Ca:TiO_2-B dual layer

sample of the same sizes using exactly the same routine and rates, determine the specific capacity of Ca:TiO_2-B at each rate first, calculate the capacity contribution of the Ca:TiO_2-B layer in the dual layer sample from its thickness obtained by STEM, and finally subtract that part from the total capacity.

For thin films grown on insulating $SrTiO_3$ substrates and using the top current collection configuration, the substrate is not a part of the electrochemical reaction or the circuit, so its contribution to the measured capacity should be minimal and hence was not considered. To test the effectiveness of the experimental setup, cyclic voltammograms (CVs) of the TiO_2-B thin film sample were recorded at scan rates from 0.1 to 1 mV s^{-1} as shown in Figure S4a. A pair of redox peaks at 1.54 V and 1.69 V were observed, which represents the signature pseudocapacitive Li^+ storage behavior of TiO_2-B.[3,4] We have calculated the specific capacitance by integrating the CVs and found the capacitance is almost the same from either the oxidation or the reduction curve, regardless of scan rate, which also corresponds well with the specific capacity obtained from galvanostatic cycling, as shown in Figure S4b. Such results directly prove the validity of our testing methods.

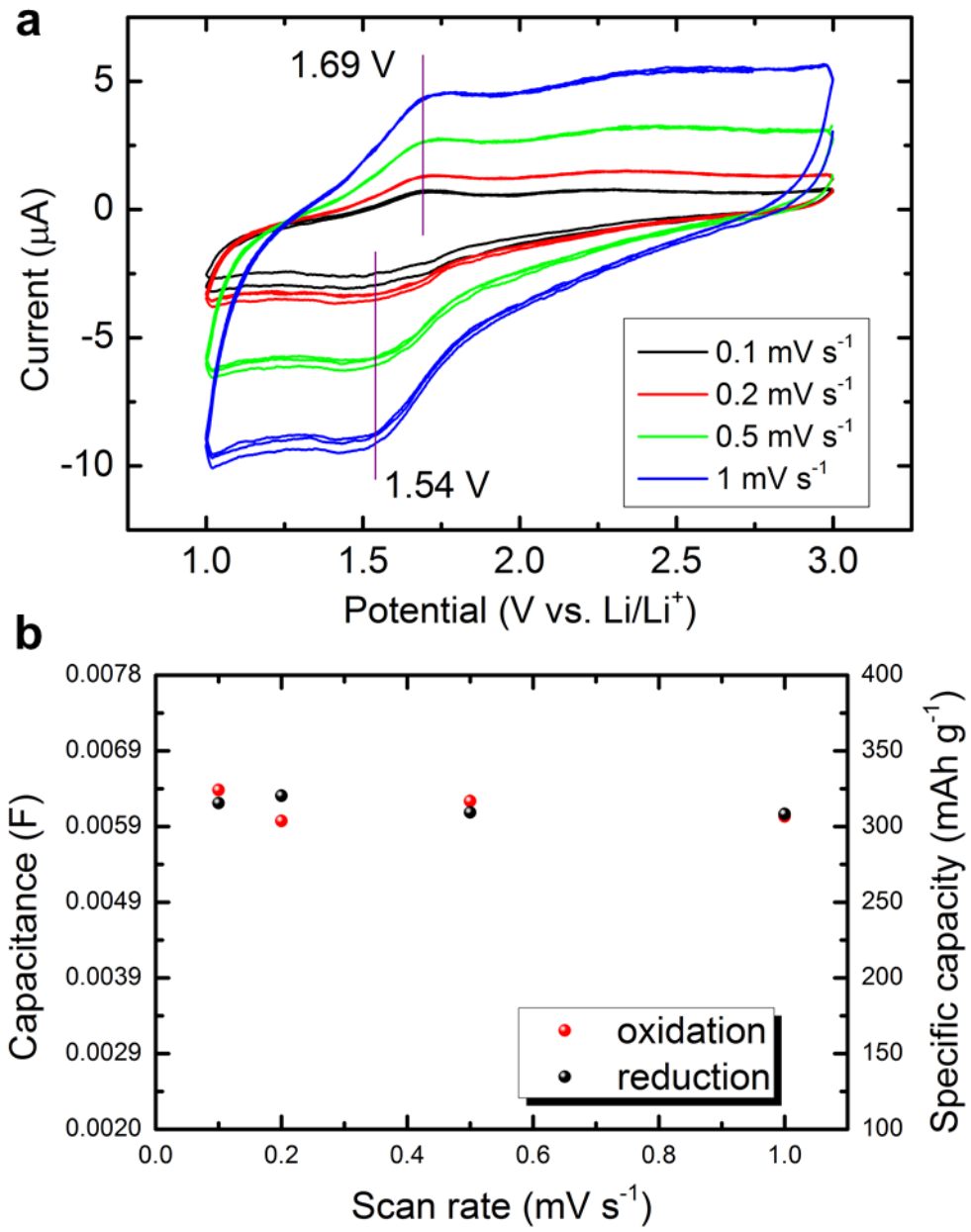

Figure S4. a) Cyclic voltammograms (CVs) of a (001) TiO_2-B thin film using the top Cu grid current collector at different scan rates. Three cycles are shown for each rate, demonstrating good repeatability of the measurement. Signature TiO_2-B peaks were observed. b) Specific capacitance calculated by integrating the CVs at different scan rates for both the oxidation and reduction curves.

For the purpose of comparing the effectiveness of these two configurations described above, two TiO_2-B/Ca:TiO_2-B dual layer control samples were grown simultaneously to the same

thicknesses on a (100) $SrTiO_3$ substrate and a (100) 0.5 at.% Nb:$SrTiO_3$ substrate, respectively. XRD and TEM results confirmed that the two films were of almost equal quality. The former was processed in a top current collection geometry as in Figure S2. Both samples, together with a bare Nb:$SrTiO_3$ substrate, were then assembled in half-cells with metallic Li counter electrodes and tested under 1C and 10C rates for 100 cycles. The discharge capacities of TiO_2-B obtained in the two samples are compared in Figure S5. It is clear that the two test configurations produced similar results, while the capacity values acquired from the top Cu grid method were slightly higher. This is due to the fact that Cu metal provides better current collection efficiency than Nb:$SrTiO_3$ semiconductor substrate. Such an advantage will become more significant as the rates increase beyond 10C. Therefore, results of battery cycling performance reported in the paper were all acquired in the top Cu grid collector configuration.

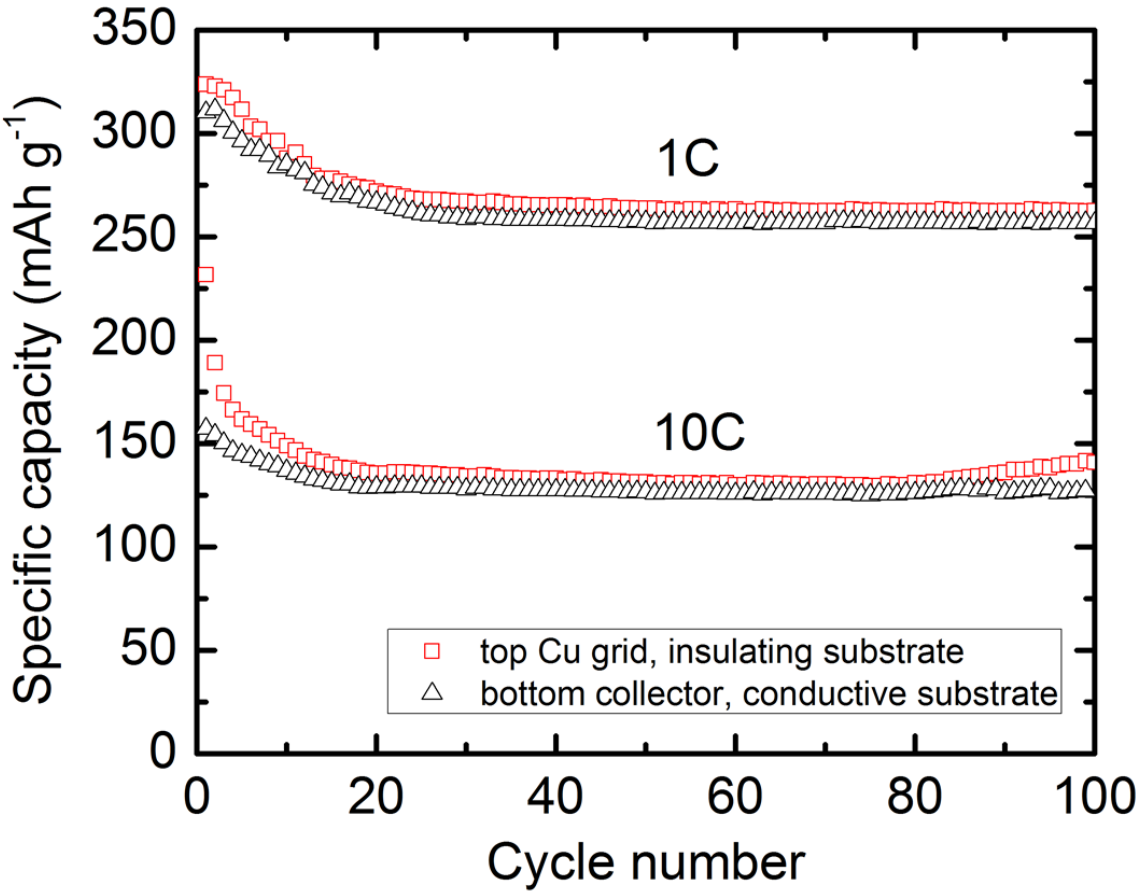

Figure S5. Comparison of discharge capacities of the TiO_2-B thin film using two different test configurations. Capacity contribution from the Ca:TiO_2-B template layer was subtracted in both configurations; capacity of the conductive Nb:$SrTiO_3$ substrate was subtracted for the bottom collector configuration.

Recent studies demonstrated that Li plating may occur at the interface of electrolyte and Cu current collector,[5] which would result in erroneously higher capacity measured for the Li storage material in battery cycling tests. To rule out the influence of possible Li plating on the Cu grid, a Ca:TiO_2-B thin film sample with top Cu grid current collector was charged and discharged at the rate of 1000C for 20 cycles, taken out of the cell at a half cycle when the film was fully charged with Li^+, and examined with an FEI Quanta scanning electron microscope. The surface image and the X-ray energy dispersive spectrum from the Cu wire are shown in

Figure S6. No obvious Li dendrite formation was observed either on the Cu wire or on the Ca:TiO_2-B film.

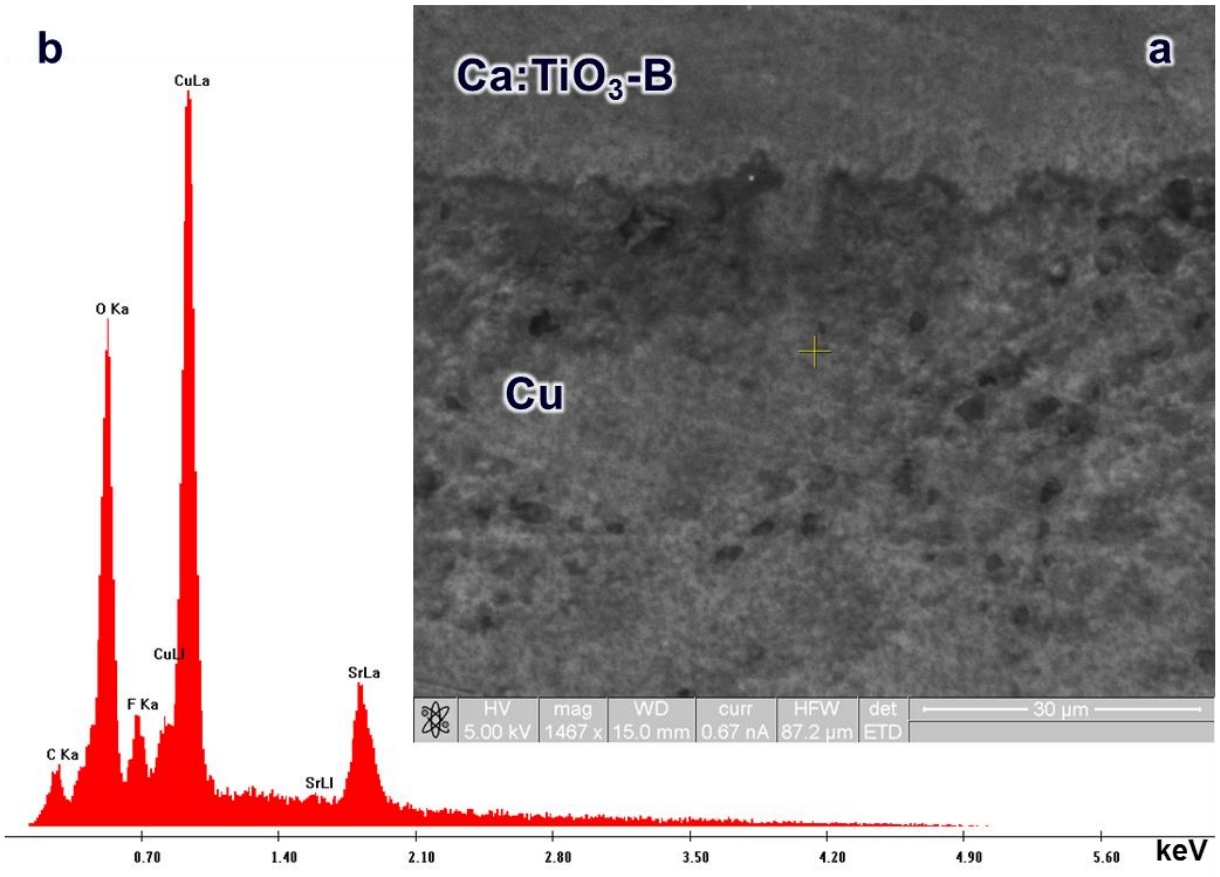

Figure S6. Cu grid surface at the charged state. a) Scanning electron microscopy image showing the surface of the Cu wire on the same Ca:TiO_2-B thin film as in Figure 3. This film was fully charged with Li^+ at the rate of 1000C, and removed from the cell at a half cycle to be examined. No obvious Li plating was observed. b) X-ray energy dispersive spectrum taken on the Cu wire. Carbon and fluorine are from the residue of $LiPF_6$ electrolyte.

Slow charge/discharge cycling experiments at a C/10 rate have been performed on a Ca:TiO_2-B film and a TiO_2-B film (with a thin Ca:TiO_2-B template layer) both grown on (100) SrTiO3 substrates using the top Cu grid collector as shown in Figure S2. The voltage profiles are displayed in the inset of Figure 4a. Both samples exhibit sloped profiles corresponding to a pseudocapacitive process of Li^+ transport, which is a typical characteristic often observed for

TiO_2-B.[4,6,7] These results also support that both the TiO_2-B and the Ca:TiO_2-B films have good purity without a pronounced amount of other TiO_2 polymorphs, which would otherwise create plateaux in the profiles.[4]

IV. Effects of battery cycling on the bronze structures

In an effort to confirm that Li^+ was actually inserted into the bronze films during cycling, fine XRD scans were performed on a (001) Ca:TiO_2-B film grown on a (100) $SrTiO_3$ substrate around the strongest available diffraction peak, 006, before and after charging with Li^+ at a rate of C/10. The results are shown in Figure S7a. Using the $SrTiO_3$ substrate peaks as reference, the 006 peak of the lithiated film has shifted to lower 2θ angles, indicating a lattice expansion in the out-of-plane direction from $c_{Ca:TiO2\text{-}B}$=17.98 Å to 18.04 Å. By fitting the experimental data, it is also clear that the peak has broadened as the inserted Li^+ disturbs the crystallinity of the lattice structure. The broadening is mainly caused by local straining within the thin film as the unit cell undergoes an asymmetric deformation upon lithiation. Structural defects such as dislocations and stacking faults may also contribute to straining effects in close regions and thus to the peak broadening.

The same experiments were performed around the TiO_2-B 001 peak of a (001) TiO_2-B/Ca:TiO_2-B dual layer film grown on a (100) $SrTiO_3$ substrate. Figure S7b shows that $c_{TiO2\text{-}B}$ exhibits a slight contraction of ~0.21% upon lithiation, which is in good agreement with the literature,[8] where neutron diffraction results revealed a contraction in $c_{TiO2\text{-}B}$ of 0.18% - 0.49%, depending on the Li content. An obvious peak broadening was again observed. Changes in the other lattice constants were not examined.

It should be noted that the lattice constant changes we observed with this post-mortem procedure may not correspond to fully lithiated films. The thin films have a large surface and a small mass, so an unknown amount of Li charged into the film could be lost to more stable lithium oxides forming on the surface when the sample was exposed to air and the electrode was examined. Although this might also happen in the more typical powder samples of TiO_2-B, the much larger amount of active material used there may ensure that more of the Li is retained in the sample.

Such a difference in sample geometry may help explain the discrepancy between our observation and the reported values in the literature. Water and anatase impurities may also have an effect on the values reported for TiO_2-B in the literature.

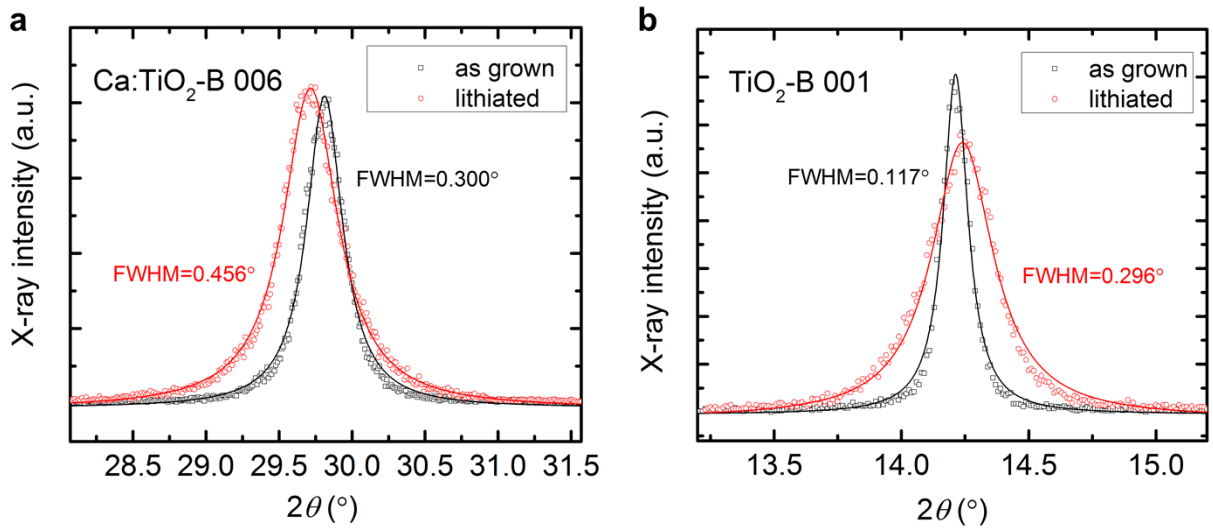

Figure S7. Lattice changes due to Li^+ intercalation. XRD fine scans of (001) bronze films grown on (100) $SrTiO_3$ substrates. Solid curves are fittings of the experimental data. a) The 006 peak of a Ca:TiO_2-B film. A peak position shift indicating an increase of *c* and a peak broadening (FWHM: full width at half maximum) were observed. b) The TiO_2-B 001 peak of a TiO_2-B/Ca:TiO_2-B dual layer film. A peak position shift indicating a slight decrease of *c*, and a peak broadening were observed.

As discussed in Figure 4c, the larger volumetric changes of the anatase walls in the TiO_2-B films can fracture the structure during Li^+ insertion and extraction. Figure S8 shows a wider area of the same film, where such fracturing always occurs along the inclined anatase walls throughout the film, some at the interface of TiO_2-B and Ca:TiO_2-B and others inside the TiO_2-B phase. Therefore, this should be an actual effect of the Li^+ insertion and extraction rather than an incidental event. A longer fracture could form between two parallel anatase walls. Because of the layered structure of TiO_2-B, all fractures are parallel to the *a*-*b* planes.

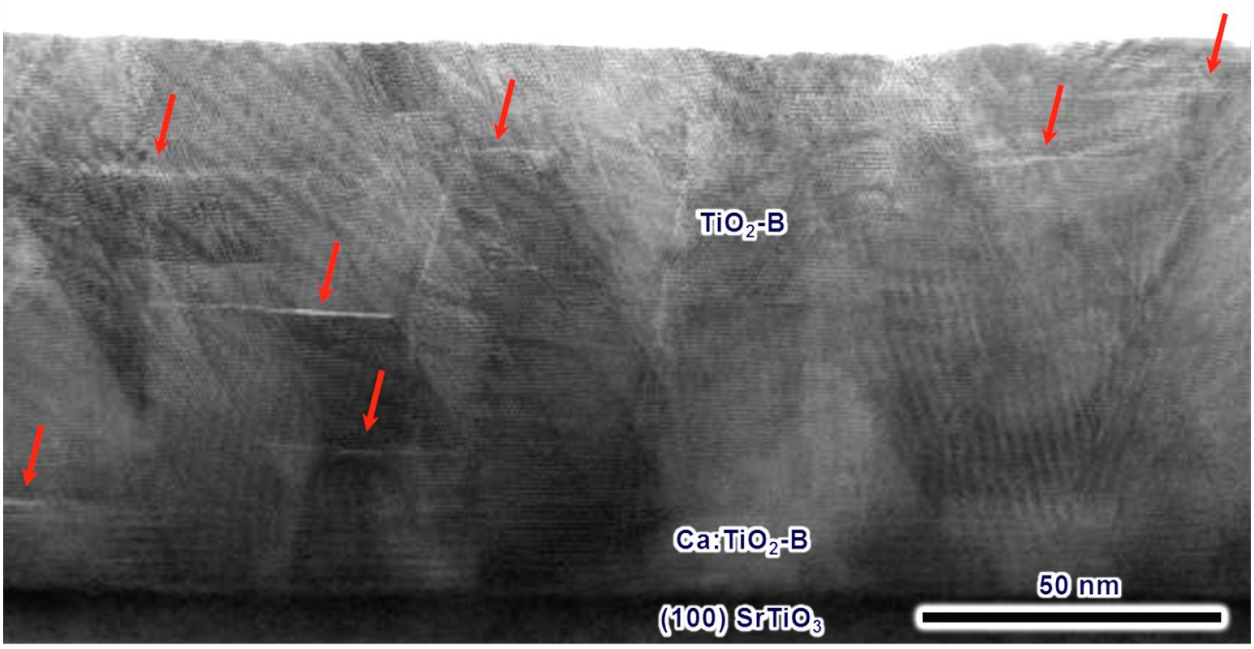

Figure S8. Fractures throughout the film caused by charging and discharging: lower magnification STEM image of the same sample as in Figure 4c showing more fractures in the TiO_2-B/Ca:TiO_2-B dual layer film after cycling. The red arrows point to some of the fractures.

References

[1] S.-i. Nishimura, G. Kobayashi, K. Ohoyama, R. Kanno, M. Yashima, A. Yamada, *Nat. Mater.* **2008**, *7*, 707.
[2] D. C. Johnson, A. L. Prieto, *Journal of Power Sources* **2011**, *196*, 7736.
[3] V. Augustyn, J. Come, M. A. Lowe, J. W. Kim, P. L. Taberna, S. H. Tolbert, H. D. Abruna, P. Simon, B. Dunn, *Nature Materials* **2013**, *12*, 518.
[4] S. Liu, H. Jia, L. Han, J. Wang, P. Gao, D. Xu, J. Yang, S. Che, *Advanced Materials* **2012**, *24*, 3201.
[5] F. Sagane, R. Shimokawa, H. Sano, H. Sakaebe, Y. Iriyama, *Journal of Power Sources* **2013**, *225*, 245.
[6] V. Etacheri, Y. Kuo, A. Van der Ven, B. M. Bartlett, *Journal of Materials Chemistry A* **2013**, *1*, 12028.
[7] S. Brutti, V. Gentili, H. Menard, B. Scrosati, P. G. Bruce, *Advanced Energy Materials* **2012**, *2*, 322.
[8] A. R. Armstrong, C. Arrouvel, V. Gentili, S. C. Parker, M. S. Islam, P. G. Bruce, *Chemistry of Materials* **2010**, *22*, 6426.